

## Multiscale Framework for Imaging Radiolabeled Therapeutics

Arutselvan Natarajan,<sup>†</sup> Silvan Türkcan,<sup>‡</sup> Sanjiv S. Gambhir,<sup>†</sup> and Guillem Pratz<sup>\*‡</sup>

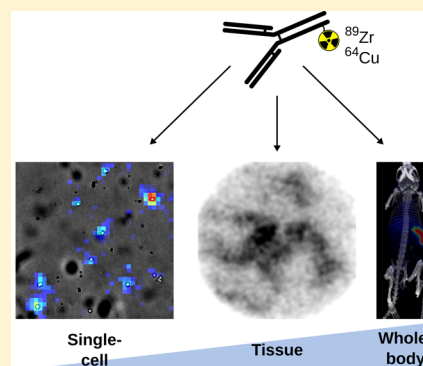
<sup>†</sup>Department of Radiology, Stanford University School of Medicine, 318 Campus Drive, Stanford, California 94305-5427, United States

<sup>‡</sup>Department of Radiation Oncology, Stanford University School of Medicine 1050 Arastradero Rd, Palo Alto, California 94304-5591, United States

### S Supporting Information

**ABSTRACT:** The resistance of a tumor to a drug is the result of bulk properties of the tumor tissue as well as phenotypic variations displayed by single cells. Here, we show that radioisotopic detection methods, commonly used for tracking the tissue distribution of drug compounds, can be extended to the single-cell level to image the same molecule over a range of physical scales. The anticancer drug rituximab was labeled with short-lived radionuclides ( $^{89}\text{Zr}/^{64}\text{Cu}$ ) and its accumulation at the organ level was imaged using PET in a humanized transgenic mouse model of non-Hodgkin's lymphoma. To capture the distribution of the drug at a finer scale, tissue sections and single living cells were imaged using radioluminescence microscopy (RLM), a novel method that can detect radionuclides with single-cell resolution. In vivo PET images (24 h postinjection) showed that [ $^{89}\text{Zr}$ ]rituximab targeted the intended site of human CD20 expression, the spleen. Within this organ, RLM was used to resolve radiotracer accumulation in the splenic red pulp. In a separate study, RLM highlighted marked differences between single cells, with binding of the radiolabeled antibody ranging from background levels to 1200 radionuclides per cell. Overall, RLM images demonstrated significantly higher spatial resolution and sensitivity than conventional storage-phosphor autoradiography. In conclusion, this combination of PET and RLM provides a unique opportunity for exploring the molecular mechanism of drugs by tracking the same molecule over multiple physical scales, ranging from single living cells to organs substructures and entire living subjects.

**KEYWORDS:** radioisotope, positron emission tomography, single cell pharmacokinetics, autoradiography



### INTRODUCTION

Tracking biomolecules as they interact with live single cells remains a challenge with current methods. The fluorophores used in fluorescence microscopy are bulky and known to interfere with the intrinsic activity of the target molecule.<sup>1</sup> Raman-based methods can track unlabeled biomolecules but are much less sensitive overall.<sup>2,3</sup> Finally, mass-spectroscopy approaches are destructive and not compatible with live-cell longitudinal or multimodal analyses. Radiolabeling approaches, despite having been established many decades ago, remain the gold standard for quantifying molecular targets at trace levels. Indeed, the process of radioactive decay releases enough energy for single radiolabeled molecules to be detected with high sensitivity, using bulk methods such as scintillation counting (in vitro) or positron emission tomography (PET; in vivo). Recently, we have shown that radionuclide detection is not limited to bulk samples, and can be applied to image molecular transport by single cells using a technique called radioluminescence microscopy (RLM).<sup>4,5</sup>

Here, we report on the use of radiolabeling for quantitatively tracking a drug over multiple physical scales, ranging from single cells to whole organisms. Whole-body autoradiography and scintillation counting are routinely used by the pharmaceutical industry to determine tissue distribution of

radiolabeled drugs, which is required to support the selection of new drug candidates and for regulatory approval.<sup>6,7</sup> However, these tools have insufficient spatial resolution to discern variations in how drugs interact with various cell types, which is important to elucidate cellular mechanisms of drug action. Microautoradiography has been employed for this purpose, but the technique, which relies on thin photographic emulsions, is extremely difficult to implement, has low sensitivity and linearity, and is not compatible with live cells.<sup>8</sup> Our recently developed method, RLM, solve these issues by employing an inorganic scintillator crystal rather than a thin emulsion. By exploiting the sectioning power of optical microscopes, a scintillator achieves a level of spatial resolution comparable to a thin emulsion. This is because although the scintillator is hundreds of microns thick, only a thin 10  $\mu\text{m}$  layer is in focus. Using this method, it is possible to localize radioactive decays in real time, in live cells, directly inside an optical microscope (Figure 1A and Supporting Information Video 1). This type of microscopy is also fully compatible with standard imaging

**Received:** May 20, 2015

**Revised:** October 1, 2015

**Accepted:** October 13, 2015

**Published:** October 13, 2015

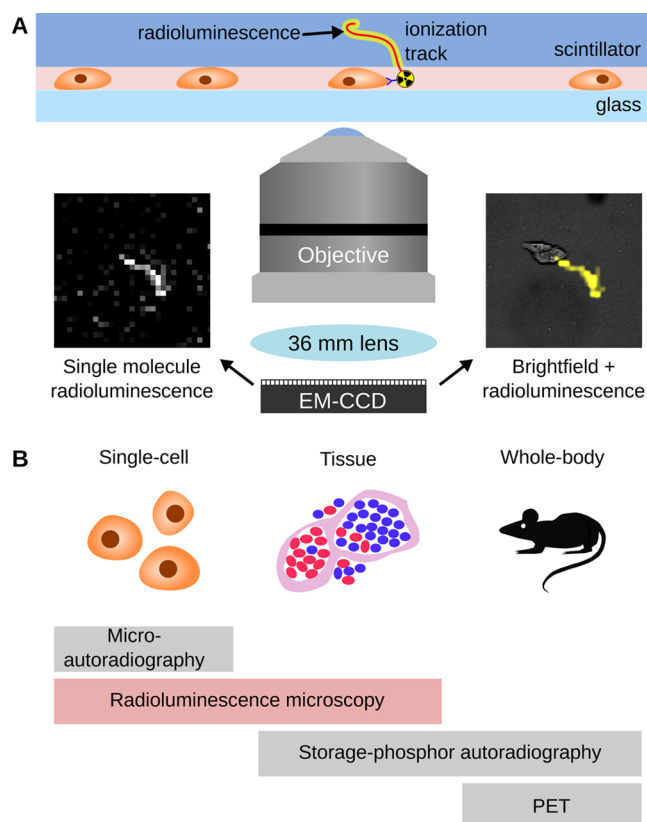


**Figure 1.** (A) Simplified diagram of the radioluminescence microscope. The microscope is composed of an objective (40 $\times$ , 1.3 NA or 20 $\times$ , 0.75 NA) coupled to a 36 mm focal-length tube lens and to an EM-CCD camera. This combination of high-NA objective and short-focal-length tube lens maximizes image brightness. Beta particles, emitted from decaying radionuclides, excite a scintillator plate placed over the sample. The radioluminescence light resulting from the decay of single molecules is visualized by the microscope (left inset). The track of a single  $\beta$  particle in the scintillator can be clearly distinguished. The position of the original decaying molecule can be inferred from this image. The matching bright-field image (right inset) confirms that the detected molecule was bound to a specific cell. By acquiring many such tracks, an image of the radionuclide distribution can be reconstructed. (B) Multiscale strategy for quantitative imaging of radiolabeled drugs, combining radioluminescence microscopy for live cell pharmacokinetics and high-resolution tissue imaging, and PET for dynamic whole-body pharmacokinetics.

techniques such as bright-field and fluorescence and can be used in conjunction with immunohistochemistry methods.

Drug resistance can be explained by individual variations between patients but also cellular differences within tumors, even when cells originate from the same tissue.<sup>9</sup> These stochastic genetic and epigenetic variations give certain cells within the tumor the ability to elude chemotherapy. Subject to intense pressure from anticancer drugs, these resistant cells have a selective advantage that allows them to regrow a tumor that is resistant to multiple classes of therapies. Understanding how drug uptake and residence time varies from one cell to another is therefore paramount for improving cancer therapies. Conventional bulk measurements, due to the averaging effect, cannot analyze the behavior of the small fraction of cells that survive chemotherapy. There is ample evidence in many cancers of a small subpopulation of tumorigenic cells that are more resistant to chemotherapy.<sup>10</sup> RLM is a promising technique for such studies because the same drug conformation

can be measured quantitatively over multiple physical scales, ranging from cells to whole organisms, thus avoiding any inconsistencies between studies (Figure 1B). Fluorescence methods too have been used to assess single-cell and subcellular pharmacokinetics,<sup>11–14</sup> but a recurring issue is that fluorophore labeling can interfere with the biological action and biodistribution of a drug molecule.

## MATERIALS AND METHODS

**Radiochemical Probe Synthesis.** The chelators *P*-isothiocyanatobenzyl-desferrioxamine (Df-Bz-NCS) and 1,4,7,10-tetraazacyclododecane-*N,N',N'',N'''*-tetraacetic acid mono-*(N*-hydroxysuccinimidyl) ester (DOTA-NHS), and the antibody rituximab (Rituxan; 10 mg/mL; 0.07 mM) were purchased from Macrocyclics (Dallas, TX, U.S.A.) and Stanford University Hospital Pharmacy (Stanford, CA, U.S.A.), respectively. Prior to conjugation of DOTA-NHS or Df-Bz-NCS (Df), two lots of rituximab (250  $\mu$ L each) were buffer-exchanged with 0.1 M phosphate buffer (pH 7.0) for DOTA-NHS, and with 0.1 M Na<sub>2</sub>CO<sub>3</sub> (pH 9.0) for Df-Bz-NCS. The buffer-exchanged rituximab (DOTA-NHS, 34  $\mu$ L, or Df-Bz-NCS, 26  $\mu$ L) and a 5 mM solution of DMSO were mixed (10 and 7.5-fold molar excess of rituximab, respectively) in a 1.5 mL Eppendorf vial. This reaction mixture was then made up to 0.4 mL of 0.1 M sodium phosphate buffer (pH = 8.5 for Df conjugation and pH = 7.5 for DOTA conjugation) and kept at room temperature for 1 h. A Slide-A-Lyzer 30 kDa cutoff membrane dialyzer (PIERCE, USA) 0.1 M sodium acetate buffer (pH 7.0) for buffer exchange was used to remove excess Df or DOTA from the reaction mixture and tested by HPLC to verify any traceable amount of chelates.

To synthesize [<sup>89</sup>Zr]rituximab, labeling reagents were added in the following sequence in a 1.5 mL Eppendorf tube. First, <sup>89</sup>Zr (90–100 MBq; 750  $\mu$ L; University of Wisconsin, Madison, WI) and 2.5 M Na<sub>2</sub>CO<sub>3</sub> (100  $\mu$ L) were mixed into the tube and kept at room temperature (RT) to balance pH. After 3 min, in the same reaction vial, 10 mM ammonium acetate buffer (150  $\mu$ L, pH 7.0), and Df-rituximab (250  $\mu$ L, 100  $\mu$ g) in 10 mM ammonium acetate buffer (pH 7.0) was added and shaken on a test tube rocker for 45 min at RT. After incubation, 0.1 M diethylenetriaminepentaacetic acid (DTPA), pH 7.0, was added to the reaction mixture to achieve final concentration of 5 mM and kept for 15 min to scavenge unchelated <sup>89</sup>Zr.

The radiolabeling of (DOTA)-rituximab with <sup>64</sup>Cu was carried out as follows: 0.2 mg of (DOTA)-rituximab was added to ~200  $\mu$ L of 0.1 M sodium acetate buffer (pH 5.5  $\pm$  1.0), and reacted with 370  $\pm$  74 MBq of (pH 7) <sup>64</sup>CuCl<sub>2</sub> solution (University of Wisconsin, Madison, WI, U.S.A.) at 37  $^{\circ}$ C for 60 min. After incubation, 0.1 M EDTA (10–120  $\mu$ L) was added and incubated at room temperature for 15 min to scavenge unchelated <sup>64</sup>CuCl<sub>2</sub> in the reaction mixture.

Radioimmunoconjugates were purified by the SEC-3000 column using Radio-HPLC with UV at 280 nm. Quality assurance of the radiotracer performed by the radio-HPLC showed greater than 95% purity, with high specific activity (1.1 MBq/ $\mu$ g for [<sup>64</sup>Cu]rituximab and 0.4 MBq/ $\mu$ g for [<sup>89</sup>Zr]-rituximab).

Additional information about the synthesis and validation of these two radiotracers has been published elsewhere.<sup>15–17</sup>

**Single-Cell Model of NHL.** A single-cell binding assay was performed using [<sup>64</sup>Cu]rituximab. The Ramos cell line (CD20+ B-cell lymphoma) was obtained from the American Type Culture Collection (ATCC number: CRL-1555). Cell labeling

was performed in a V-bottomed 96-well microtiter plate. In a single well, 100  $\mu\text{L}$  of the [ $^{64}\text{Cu}$ ]rituximab (10 ng/mL, optimized) was mixed with 100  $\mu\text{L}$  of  $5.5 \times 10^6$  Ramos cells and incubated for 2 h at 37°. The antibody-coated cells were washed thrice with 1% PBSA, and then prepared for imaging.

For validation purpose, the [ $^{64}\text{Cu}$ ]rituximab-labeled cells were stained with a secondary antibody against rituximab. Rituximab-coated cells were washed thrice with FACS buffer, followed by each well receiving 100  $\mu\text{L}$  of goat antihuman IgG/Fc-FITC (Jackson ImmunoResearch, West Grove, PA) prediluted to 1:100 in FACS-buffer. Cell staining was performed in the dark on ice for 0.5 h and followed by a triple wash with FACS buffer.

**In Vivo Model of NHL and PET Imaging.** The huCD20 transgenic mice used in the experiments were purchased from Genentech (South San Francisco, CA). These mice were engineered to express the human CD receptor (huCD20) on B cells. To confirm the expression of huCD20, the mice were screened by the reverse-transcription polymerase chain reaction (RT-PCR) analysis. Animal experiments were performed with approval from the Administrative Panel on Laboratory Animal Care (APLAC) at Stanford University. Two groups of huCD20 transgenic mice ( $n = 3$ , average weight of  $25.0 \pm 2.0$  g) were selected. These mice received  $2.8 \pm 0.2$  MBq of  $^{89}\text{Zr}$ -Df-rituximab [200  $\mu\text{L}$ ] via tail vein injection. After a single tracer administration, the animals were scanned at 4, 24, 48, and 72 h using a small-animal PET/CT at the Stanford small animal imaging center (Siemens Inveon; standard acquisition and reconstruction settings).

After completion of the small-animal PET study (72 h post injection), the spleen of one of the mice was resected, frozen, and sectioned axially using a microtome (10  $\mu\text{m}$  slice thickness). To allow for a direct comparison, the same tissue slice was imaged sequentially using RLM and autoradiography. Hematoxylin and eosin (H and E) staining was performed on a contiguous slice.

**Radioluminescence Microscopy.** A detailed description of the RLM is available elsewhere.<sup>4</sup> Briefly, a bioluminescence microscope (LV200, Olympus) was used to capture the position of individual positrons emitted during radionuclide decay. The microscope comprises: an electron-multiplying charge-coupled device (EMCCD) camera (ImageEM C9100-14, Hamamatsu) operating at maximum gain with  $4 \times 4$  pixel binning; a microscopy objective, either 40 $\times$ , 1.3 NA (UPLFLN40XO, Olympus) or 20 $\times$ , 0.75 NA (UPLSAPO20X, Olympus); and a custom high-brightness 0.2 NA, 36 mm-focal-length tube lens.<sup>18</sup> Owing to the short focal length of the tube lens, the effective magnification of the microscope is one-fifth of the magnification specified by the objective, that is, 8 $\times$  and 4 $\times$ , respectively.

To convert the energy released during radioactive decay into light, a transparent scintillator ( $\text{CdWO}_4$ , two-side polished, 1 cm  $\times$  1 cm  $\times$  0.5 mm; MTI Corp., Richmond, CA) was placed in contact with the sample to be imaged. For tissue imaging, the freshly sectioned tissue was dropped directly onto the scintillator, allowed to dry, and then placed face-down in a glass-bottom imaging dish. For single-cell imaging, the cells were suspended in cold matrigel and a small drop (10  $\mu\text{L}$ ;  $2.7 \times 10^5$  cells) was deposited between a glass-bottom imaging dish and the scintillator.

Acquisition of RLM images was performed as follows. A sequence of frames was acquired in rapid succession using a short exposure time, with the illumination turned off. Raw

camera frames were then processed to obtain the radionuclide distribution according to our methodology called "optical reconstruction of the beta-ionization track" (ORBIT), which is described in details in a previous publication.<sup>5</sup> A major difference with our previously reported work is that we did not use the bright-field image as prior information to guide the reconstruction of the RLM image. Our experience is that prior information can bias the reconstruction by pushing background counts toward isolated cells. Furthermore, the bright-field image is not useful when imaging tissue sections because the field of view is almost entirely filled with cells. Instead, radionuclide events were first screened to remove low-quality events (out of focus, or long positron track), and then localized to the center of mass of the light distribution, regardless of the bright-field image.

For tissue imaging, two different images of the spleen were acquired at different magnifications. The 8 $\times$  image was acquired on the day the specimen was processed. To obtain a high-quality image, 65 000 frames were acquired using an exposure time of 300 ms per frame, resulting in a total exposure time of 5.4 h. A 4 $\times$  image of the same sample was recorded 3 days later. Due to the larger field of view, we observed a higher rate of radioactive decay and had to decrease the exposure time to 200 ms per frame. The number of frames was set to 65 000, resulting in a total exposure of 3.6 h.

For single-cell imaging, 43 000 frames were acquired with an exposure time of 2 s per frame, resulting in a total exposure of 24 h. The single-cell RLM images were reconstructed at a pixel resolution of 13  $\mu\text{m}$  ( $4 \times 4$  CCD binning,  $2 \times 2$  software binning, and 8 $\times$  effective magnification), with no additional interpolation or postprocessing. It is possible to reconstruct images at a higher resolution if more counts are available.

**Autoradiography.** Standard autoradiography was performed last on the same tissue slice, 6 days after excision of the spleen. A storage-phosphor screen (super-resolution, PerkinElmer) was used to record  $^{89}\text{Zr}$  radionuclide activity for 10 days at  $-20$  °C, until the radioactivity of the specimen had nearly fully decayed (equivalent to three half-lives). The latent image was read out using a laser-based scanner with 42  $\mu\text{m}$  pixel resolution (Cyclone Plus Phosphor Imager, PerkinElmer). Although the radioactivity had already decayed by 72% when autoradiography started, nearly all the remaining radioactivity was captured thanks to the long exposure time.

Autoradiography was also performed on the single-cell suspension, which was prepared as previously described. The cells were suspended in cold matrigel and a small drop (10  $\mu\text{L}$ ;  $2.7 \times 10^4$  cells) was deposited between a glass slide and the storage-phosphor film. Gentle pressure was applied to ensure close contact between the cells and the film. Cell concentration was set deliberately 10 times lower than for RLM due to the limited spatial resolution of storage-phosphor autoradiography. The sample was exposed for 24 h and read out using the Cyclone Plus Phosphor Imager. The pixel size was set to 42  $\mu\text{m}$  (600 dpi), which is sufficient since the spatial resolution of the system is approximately 200  $\mu\text{m}$  (2.5 line pairs per millimeter). No postprocessing was applied to the image, except for basic intensity windowing.

**Fluorescence Microscopy.** Fluorescence microscopy was performed on the LV200 microscope, with the scintillator still in place. A green fluorescent protein (GFP) filter set was used. The LV200 operates in transillumination mode, using a tungsten white light source. Because of this rudimentary design, the images suffer from a high level of filter bleed-

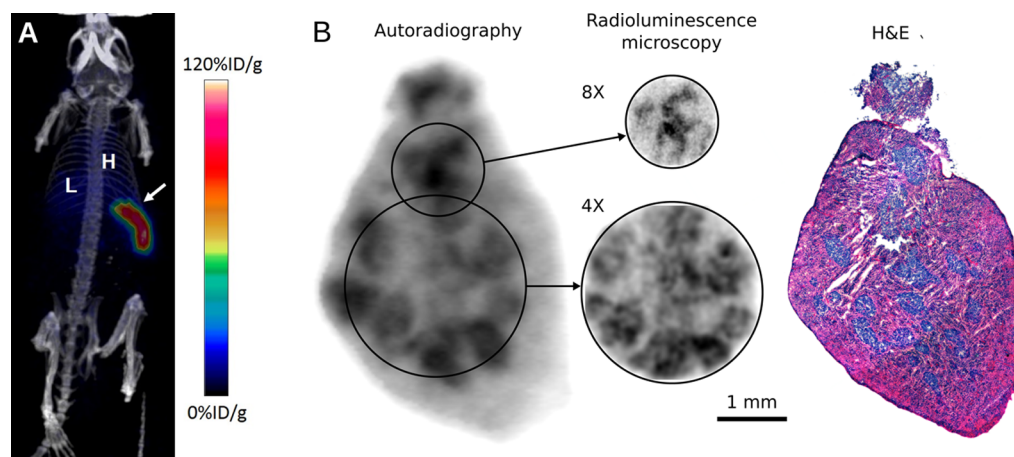


**Figure 2.** (A) In vivo imaging of cancer therapeutics. In vivo PET imaging was used to establish organ-level pharmacokinetics of the radiolabeled compound,  $^{89}\text{Zr}$ -rituximab (78 h half-life). The compound was imaged in a murine model of non-Hodgkin's lymphoma. (B) Tissue-level heterogeneity was then measured ex-vivo in frozen tissue sections using RLM (4 $\times$  and 8 $\times$ ), and compared to storage-phosphor autoradiography, the standard method. The higher spatial resolution is clearly visible.

through, which was estimated numerically and removed. A field flatness factor was estimated by imaging a uniform distribution of fluorescein and used to correct the flatness of the fluorescence image. Fluorescence images were acquired with no pixel binning, an EM gain of 701, and an exposure time of 30 s. The fluorescence images are naturally coregistered with the RLM images because the same camera is used for both modalities.

**Analysis of Single Cells Images.** For absolute quantitation of [ $^{64}\text{Cu}$ ]rituximab in single cells using RLM, a reference scan was performed by imaging a known amount of  $^{18}\text{F}$  radionuclide, which was uniformly spread as a thin sheet (Supporting Information Figure 1). This reference scan allowed us to convert the observed radionuclide counts into absolute drug concentration. Using the bright-field image as a reference, we measured the position of 44 single cells, which excluded cells that were part of dense clusters. Because the bright-field and RLM images are coregistered, we placed circular regions of interest (ROIs; diameter 32.5  $\mu\text{m}$ ) around each single cell, using the bright-field image as a guide. We applied these ROIs to the RLM image to compute the number of radionuclide counts detected per cell. For the purpose of background correction, background counts were estimated by placing circular regions of interest in areas of the bright-field image devoid of cells. For each single cell, the absolute number of  $^{64}\text{Cu}$  atoms  $N$  is calculated from the number  $C$  of observed radioactive counts using the following formula:

$$N = \frac{C/YS}{1 - \exp(-\lambda T)}$$

This calculation accounts for the exponential decay rate  $\lambda$  of the  $^{64}\text{Cu}$  radionuclide (half-life = 12.7 h), the duration  $T$  of the exposure, the sensitivity  $S$  of the RLM instrument (30%), and the radioactive yield  $Y$  of  $^{64}\text{Cu}$ , which decays according to a complex scheme yielding positrons (17%), electrons (39%), or no detectable particle (electron capture).

As a reference, average cell binding of [ $^{64}\text{Cu}$ ]rituximab was also estimated using a bulk gamma counter (Cobra II, Packard). Briefly, measurements were performed in triplicate using approximately 5.5 million cells per vial and an exposure time of 1 min. Count numbers were converted into absolute radioactivity using a calibrated reference ladder. The average

radioactivity per cell was then computed as the ratio of the bulk radioactivity to the number of cell in each vial (estimated using a hemocytometer).

To estimate spatial resolution, the apparent size of single cells was measured on the RLM and ARG images by fitting the profiles of individual single cells with a 2D Gaussian function. This was done using a nonlinear least-squares solver in MATLAB. The apparent cell size is defined as the full width at half maximum of the Gaussian distribution. The true cell size was also estimated on the bright-field image by averaging the vertical and horizontal diameter of the cell.

## RESULTS

We applied the concept of multiscale imaging to rituximab, a monoclonal antibody used to treat hematological malignancies such as non-Hodgkin's lymphomas (NHL). The drug was labeled with  $^{89}\text{Zr}$ , a positron emitter with a 78 h half-life, using a previously developed conjugation strategy.<sup>16</sup> The tissue distribution of the radiolabeled drug was first imaged in a humanized transgenic mouse model of NHL (huCD20+) using small-animal PET. Images taken 72 h after injection show that the drug is retained primarily in the spleen, as expected for this animal model (Figure 2A). Competitive blocking with a predose of cold rituximab confirmed the high specificity of the radionuclide-antibody conjugate (Supporting Information Figure 2).

In order to visualize the drug distribution at the organ level, the spleen was resected, and frozen sections were imaged both using standard storage-phosphor autoradiography and RLM. Both approaches demonstrated that the drug was confined to the red pulp fraction of the spleen, the principal site of accumulation of huCD20+ lymphocytes (Figure 2B). RLM had noticeably higher spatial resolution than autoradiography, evidenced by the sharper images. This is because RLM acquires and reconstructs images using a super-resolution method, which removes the blurring caused by the travel of the positrons. Furthermore, although the phosphor screen was exposed for 10 days to allow the radioactive specimen to decay almost entirely, the RLM exposure took only a few hours. Specifically, the RLM images required 80% (4 $\times$ ) and 93% (8 $\times$ ) fewer radioactive decays than autoradiography, yet displayed much sharper features at a comparable level of noise. This

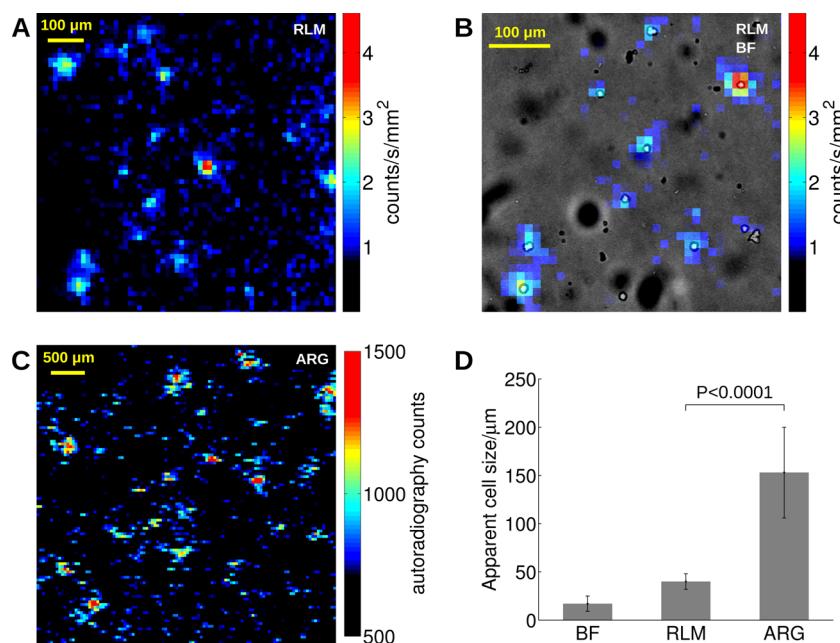


**Figure 3.** Autoradiography of single cells. (A) High-resolution RLM image of the binding of [ $^{64}\text{Cu}$ ]rituximab by single Ramos cells. (B) Detail from the RLM image, overlaid onto coregistered bright-field (BF) image, shows that focal radionuclide binding is localized within  $\approx 20\ \mu\text{m}$  of single Ramos cells. (C) Autoradiography (ARG) can also distinguish single cells (or clusters of a few cells) in highly dilute cell suspensions. As indicated by the scale bar, the ARG image is displayed at 5 $\times$  lower magnification than the RLM image. (D) Apparent cell size, measured as the full width at half maximum (fwhm) of a 2D Gaussian function.

confirms that RLM is a highly sensitive method for imaging tissue sections, which is crucially important for obtaining high-resolution images of the distribution of drugs or other compounds in tissues.

However, the full potential of RLM is truly revealed in single-cell drug binding studies. To investigate the distribution of the drug at the single-cell level, we targeted the human CD20 protein expressed on Ramos cells using [ $^{64}\text{Cu}$ ]rituximab, which was developed in a previous study.<sup>15</sup> The  $^{64}\text{Cu}$  radiometal was selected for its shorter half-life (12.7 h), more suitable than  $^{89}\text{Zr}$  for short in vitro experiments. A suspension of single labeled cells was imaged using RLM and individual cells were clearly identified (Figure 3A) and matched the location of cells on the bright-field micrograph (Figure 3B). Single cells could be distinguished using autoradiography, but only after 10 $\times$  dilution of the sample and with 2–3 times worse spatial resolution (Figure 3C; note the different scale bars). The diameter of single cells was measured on both sets of images and found to be significantly different ( $P < 0.0001$ ; Figure 3D). Cells had an apparent diameter of  $40 \pm 8\ \mu\text{m}$  on the RLM image, compared with  $153 \pm 47\ \mu\text{m}$  on the autoradiograph. Both diameters are considerably larger than the true physical diameter of the cells, which is  $17 \pm 8\ \mu\text{m}$  (according to bright-field). Furthermore, the spread of the radioluminescence signal produced by individual cells was significantly correlated ( $P = 0.003$ ; Pearson correlation  $r = 0.89$ ) with the diameter of the cell, as measured on the bright-field image (Supporting Information Figure 3). Surprisingly, for each 1  $\mu\text{m}$  increment in the cell's diameter, the spread of the RLM signal increased by 5  $\mu\text{m}$ . In contrast, the spread of the RLM signal was not significantly correlated with the amount of rituximab binding ( $P > 0.05$ ; data not shown).

Using a calibration procedure prior to imaging, we estimated the radioactivity of individual cells using the RLM image and found that it was equivalent to approximately  $5.0 \pm 0.6\ \text{mBq/}$

cell, equivalent to  $330 \pm 40\ ^{64}\text{Cu}$  atoms/cell ( $N = 44$ ; Figure 4). To validate this finding, the radioactivity of the cells was

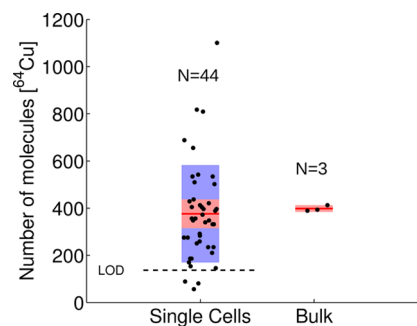


**Figure 4.** Quantitative analysis of single-cell binding of [ $^{64}\text{Cu}$ ]rituximab. (left) Quantitative region-of-interest analysis of the RLM image, showing drug binding for 44 single cells (each dot = 1 cell). The standard deviation and standard error of the mean (sem) are shown in purple and light red, respectively, and the mean is shown as a red line. (right) Bulk gamma counting, shown as a reference, confirms that both approaches measure similar levels of drug binding, on average (each dot = 5.5 million cells).

also measured independently using a bulk gamma counter and found to be  $6.0 \pm 0.1\ \text{mBq/cell}$  (Figure 4). Although both assays reported similar values for drug binding ( $16 \pm 14\%$  agreement), only RLM was able to measure cell-to-cell heterogeneity within the population. The coefficient of variation of the population was found to be 49%. Specifically, the measured values ranged from background level to  $\approx 1200\ ^{64}\text{Cu}$  atoms/cell, a 7-fold difference.

Finally, to further validate the use of RLM for single cell studies, we stained the Ramos cells with a secondary fluorescent antibody against rituximab (goat antihuman IgG/Fc-FITC). Immediately before starting RLM acquisition, we acquired a

fluorescence micrograph of the same cells using the same microscope (Figure 5A). Comparing the two images, it is clear

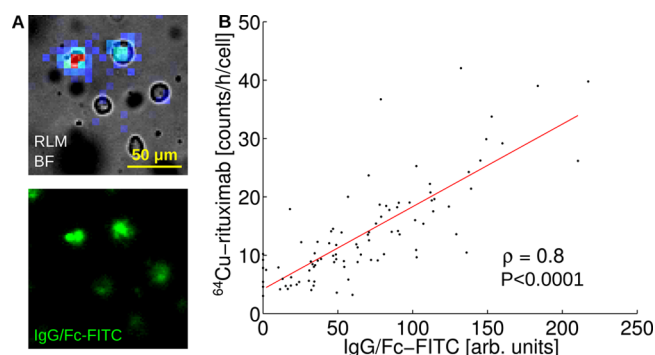


**Figure 5.** Dual fluorescence/radioluminescence imaging of [ $^{64}\text{Cu}$ ]-rituximab. (A) Radioluminescence (top) and fluorescence (bottom) micrograph of rituximab binding in Ramos cells. Cells were first stained with [ $^{64}\text{Cu}$ ]rituximab, then with a fluorescent antihuman secondary antibody against rituximab. (B) Region-of-interest analysis of single Ramos cells ( $N = 93$ ), comparing fluorescence to radioluminescence intensity. The two signals are significantly correlated (Pearson correlation coefficient,  $\rho = 0.8$ ;  $P < 0.0001$ ).

that fluorescence and radioluminescence signals originate from the same cells. Furthermore, cells that are visibly brighter on the RLM image also appear bright on the fluorescence image. This was quantified by comparing fluorescence and radioluminescence intensity for 93 single cells (Figure 5B). A strong correlation of 0.8 was found, which is statistically significant ( $P < 0.0001$ ). This finding is strong evidence that RLM signal is proportional to drug binding.

## DISCUSSION

We have demonstrated the use of PET imaging to measure in vivo pharmacokinetics at the tissue level and RLM to assess the extent to which the binding of the radiolabeled antibody varies from cell to cell. The level of heterogeneity observed in this study may be related to cellular subtypes and, thus, could play a significant role in how single cells differ in their response to therapy. Thus, the therapeutic potential of a drug is best assessed using sensitive and specific assays that operate over a wide range of physical scales (single cell, tissue, and whole-body). Furthermore, to avoid inconsistencies between different assays, the chemical conformation of the labeled molecule must be as similar as possible to the unmodified molecule.

This study confirms that RLM has ideal characteristics for imaging beta-emitting nuclides with high resolution, in a microscopy setup. The sensitivity of the system was measured using a calibration standard and was found to be approximately 30% (Supporting Information Figure 1). A precise measurement of the spatial resolution of RLM is more difficult to obtain for lack of a microscopic radioactive point source (with diameter much smaller than the resolution of the system). For  $\text{CdWO}_4$  scintillators, we estimate that spatial resolution is approximately 20–25  $\mu\text{m}$ . This is based on the observation of single cells; for instance, in Figure 5A, two cells separated by 25  $\mu\text{m}$  (membrane to membrane) are clearly distinguished on the RLM image. From a physical perspective, the sources of localization error are multiple: First, because cells are three-dimensional, beta particles can be emitted up to 15  $\mu\text{m}$  from the edge of the scintillator. The travel of the particle introduces lateral error in proportion to the vertical distance between the

scintillator and the emitting molecule. A second source of error is the finite thickness of the scintillator. Scintillation light, produced all along the track of the particle, makes it challenging to determine precisely where the particle entered the scintillator, although this effect is partially mitigated by optical sectioning. Another source of error is the limited sampling of the camera sensor, especially when  $4 \times 4$  pixel is used. Altogether, these blurring effects are consistent with an estimated spatial resolution of 20–25  $\mu\text{m}$ .

As shown in this study, conventional storage-phosphor autoradiography can be used to obtain measurements at the single-cell level (Figure 3C). However, the worse spatial resolution requires cell suspensions to be more dilute, and the low sensitivity demands longer exposures. Furthermore, autoradiography does not have the capability to perform optical microscopy to verify the position and health of single cells. For these reasons, RLM is far more adapted to single-cell analyses.

Digital autoradiography is another potential method for imaging single cells. This type of autoradiography uses a solid-state detector to directly detect incoming  $\beta$  particles without the intermediate step of converting the ionization into light.<sup>19–21</sup> This method is very efficient and sensitive and can achieve spatial resolution on the order of tens of microns for low-energy radionuclides. However, an issue of considerable importance is that digital autoradiography does not easily permit the imaging of aqueous samples, such as live cells in their media. This prevents pharmacokinetic studies from being conducted on live single cells. Additionally, from a physical perspective, most solid-state detectors are made from silicon dioxide, which has 2–3 times lower stopping power for beta particles than a dense inorganic scintillator. Therefore, the amount of ionization in a layer of a given thickness will be several-fold lower in silicon than in a dense scintillator. Finally, one last point to consider is that RLM enables microscopic examination of the same sample using optical contrasts (e.g., Figure 5), a feature not available on a digital autoradiography system. Therefore, RLM has many unique features that are not easily replicated using currently existing technologies.

The RLM methodology followed in this study is for the most part consistent with previous work,<sup>4,5</sup> with a few differences. One difference was the use of RLM for imaging tissue sections rather than single cells. We found that dropping the tissue section directly onto the scintillator was the most effective method for obtaining a high-quality image. This study is also the first reported use of the radiometals  $^{64}\text{Cu}$  and  $^{89}\text{Zr}$  for RLM. Last, by trial and error, we have also refined our imaging protocol, most notably by switching to a simpler image reconstruction method that is less prone to bias. Other than these aspects, the RLM methodology was followed as previously described.

Other recent developments in RLM can also be used for studying radiolabeled therapeutics. For instance, a microfluidic chip can be bonded to the scintillator to enable single cells to be manipulated with ease across the entire field of view of the microscope.<sup>22</sup> Additionally, microcolumnar thin-film  $\text{Lu}_2\text{O}_3:\text{Eu}$  coatings can be used as scintillators to improve the spatial resolution of RLM images in a significant way.<sup>23</sup> The higher resolution could potentially be useful for imaging tissue sections, in which cells are packed tightly in the field of view.

One of the limitations of this study was that single-cell and tissue-level imaging were not performed on the same biological system. It is currently not possible to distinguish single cells

within a tissue section with RLM, due to the limited 25  $\mu\text{m}$  resolution. In principle, the tissue could be dissociated into a single-cell suspension to spread out the cells. Instead, an in vitro model of NHL was used for the single-cell part of our study. This was due to the need to optimize the labeling of single cells for RLM imaging. The single-cell suspension was incubated with 10 kBq/mL [ $^{64}\text{Cu}$ ]rituximab for 2 h. Such a low dose was used to limit the pharmacological effects of the drug on the cells and resulted in fewer than 0.1% of the CD20 receptors<sup>24</sup> labeled. The exposure time of 24 h could be dramatically shortened by increasing the amount of labeling antibody or by using radionuclides with higher specific activity. For instance, in previous work, we have produced single-cell images of  $^{18}\text{F}$ -fluorodeoxyglucose (FDG) in 5 min<sup>4,5</sup> (incubation using 10 MBq/mL for 30 min).

RLM is a promising technique for applying radiochemical tools to single-cell and high-resolution tissue studies. Although this study focused on large antibody molecules, the method can be applied to tracking small-molecule drugs that are harder to label and detect with nonradioisotopic methods. In combination with PET, RLM opens new research avenues for performing multimodal molecular studies with high sensitivity and specificity over a wide range of physical scales, using a variety of in vitro and in vivo disease models.

## ■ ASSOCIATED CONTENT

### 📄 Supporting Information

The Supporting Information is available free of charge on the ACS Publications website at DOI: 10.1021/acs.molpharmaceut.5b00392.

RLM calibration scan, PET imaging, apparent cell size. (PDF)

Sample of 600 raw frames acquired with RLM. (MPG)

## ■ AUTHOR INFORMATION

### Corresponding Author

\*E-mail: [pratz@stanford.edu](mailto:pratz@stanford.edu). Phone: (650) 724-9829. Fax: (650) 723-7254.

### Notes

The authors declare no competing financial interest.

## ■ ACKNOWLEDGMENTS

This work was supported in part by a grant from the National Institutes of Health (R01CA186275) and by a Prostate Cancer Research Program fellowship (W81XWH-14-1-0288). Micro-PET/CT imaging and Gamma Counter measurements were performed in the SCi3 Stanford Small Animal Imaging Service Center. The LV200 microscope was loaned by the Olympus Corporation.

## ■ REFERENCES

- (1) Resch-Genger, U.; Grabolle, M.; Cavaliere-Jaricot, S.; Nitschke, R.; Nann, T. Quantum dots versus organic dyes as fluorescent labels. *Nat. Methods* **2008**, *5*, 763–775.
- (2) Wei, L.; et al. Live-cell imaging of alkyne-tagged small biomolecules by stimulated Raman scattering. *Nat. Methods* **2014**, *11*, 410–412.
- (3) Freudiger, C. W.; et al. Label-Free Biomedical Imaging with High Sensitivity by Stimulated Raman Scattering Microscopy. *Science* **2008**, *322*, 1857–1861.
- (4) Pratz, G.; et al. Radioluminescence Microscopy: Measuring the Heterogeneous Uptake of Radiotracers in Single Living Cells. *PLoS One* **2012**, *7*, e46285.

- (5) Pratz, G.; et al. High-Resolution Radioluminescence Microscopy of  $^{18}\text{F}$ -FDG Uptake by Reconstructing the beta-Ionization Track. *J. Nucl. Med.* **2013**, *54*, 1841–1846.

- (6) Solon, E. G.; Lyubimov, A. V. In *Encyclopedia of Drug Metabolism and Interactions*; John Wiley & Sons, Inc.: Hoboken, NJ, 2011.

- (7) Solon, E.; Schweitzer, A.; Stoeckli, M.; Pridaux, B. Autoradiography, MALDI-MS, and SIMS-MS Imaging in Pharmaceutical Discovery and Development. *AAPS J.* **2010**, *12*, 11–26.

- (8) Puncher, M. B.; Blower, P. Radionuclide targeting and dosimetry at the microscopic level: the role of microautoradiography. *Eur. J. Nucl. Med.* **1994**, *21*, 1347–1365.

- (9) Gottesman, M. M. Mechanisms of cancer drug resistance. *Annu. Rev. Med.* **2002**, *53*, 615–627.

- (10) Dean, M.; Fojo, T.; Bates, S. Tumour stem cells and drug resistance. *Nat. Rev. Cancer* **2005**, *5*, 275–284.

- (11) Willingham, M. C.; Cornwell, M. M.; Cardarelli, C. O.; Gottesman, M. M.; Pastan, I. Single cell analysis of daunomycin uptake and efflux in multidrug-resistant and-sensitive KB cells: effects of verapamil and other drugs. *Cancer Res.* **1986**, *46*, 5941–5946.

- (12) Koshkin, V.; Krylov, S. N. Single-cell-kinetics approach to compare multidrug resistance-associated membrane transport in subpopulations of cells. *Anal. Chem.* **2011**, *83*, 6132–6134.

- (13) Thurber, G. M.; et al. Single-cell and subcellular pharmacokinetic imaging allows insight into drug action in vivo. *Nat. Commun.* **2013**, *4*, 1504.

- (14) Laughney, A. M.; et al. Single-cell pharmacokinetic imaging reveals a therapeutic strategy to overcome drug resistance to the microtubule inhibitor eribulin. *Sci. Transl. Med.* **2014**, *6*, 261ra152.

- (15) Natarajan, A.; et al. Positron Emission Tomography of  $^{64}\text{Cu}$ -DOTA-Rituximab in a Transgenic Mouse Model Expressing Human CD20 for Clinical Translation to Image NHL. *Mol. Imaging Biol.* **2012**, *14*, 608–616.

- (16) Natarajan, A.; Habte, F.; Gambhir, S. S. Development of a Novel Long-Lived ImmunoPET Tracer for Monitoring Lymphoma Therapy in a Humanized Transgenic Mouse Model. *Bioconjugate Chem.* **2012**, *23*, 1221–1229.

- (17) Natarajan, A.; Gambhir, S. Radiation Dosimetry Study of [ $^{89}\text{Zr}$ ]rituximab Tracer for Clinical Translation of B cell NHL Imaging using Positron Emission Tomography. *Mol. Imaging Biol.* **2015**, *17*, 1–9.

- (18) Ogoh, K.; et al. Bioluminescence microscopy using a short focal-length imaging lens. *J. Microsc.* **2014**, *253*, 191–197.

- (19) Ott, R. J.; Macdonald, J.; Wells, K. The performance of a CCD digital autoradiography imaging system. *Phys. Med. Biol.* **2000**, *45*, 2011–2027.

- (20) Cabello, J.; et al. Digital autoradiography using room temperature CCD and CMOS imaging technology. *Phys. Med. Biol.* **2007**, *52*, 4993.

- (21) Esposito, M.; Mettievier, G.; Russo, P.  $^{14}\text{C}$  autoradiography with an energy-sensitive silicon pixel detector. *Phys. Med. Biol.* **2011**, *56*, 1947.

- (22) Türkcan, S.; et al. Single-Cell Analysis of [ $^{18}\text{F}$ ] Fluorodeoxyglucose Uptake by Droplet Radiofluidics. *Anal. Chem.* **2015**, *87*, 6667–6673.

- (23) Sengupta, D.; et al. Bright  $\text{Lu}_2\text{O}_3$ : Eu Thin-Film Scintillators for High-Resolution Radioluminescence Microscopy. *Adv. Healthcare Mater.* **2015**, *4*, 2064.

- (24) Law, C.-L.; et al. Efficient Elimination of B-Lineage Lymphomas by Anti-CD20–Auristatin Conjugates. *Clin. Cancer Res.* **2004**, *10*, 7842–7851.